Nano Research

Open Access

Research Article

High strength sustainable nanocomposites with multicomponent synergistic reinforcement

Guojun Che[1,2], Shuxing Yin[1,2], Cheng Qian[1,2], Can Zhou[1,2], Yi Ding[1,2], Ying Zhang[1,2], Chuangqi Zhao[1,2] ✉, and Lei Jiang[1,2]

[1] *State Key Laboratory of Bioinspired Interfacial Materials Science, School of Chemistry and Materials Science, University of Science and Technology of China, Hefei 230026, China*
[2] *Suzhou Institute for Advanced Research, University of Science and Technology of China, Suzhou 215123, China*

Cite this article: *Nano Research*, **2026**, *19*, 94908491. https://doi.org/10.26599/NR.2026.94908491

ABSTRACT: Plastics play an indispensable role in daily life, but their adverse impacts on nature and human health are becoming increasingly severe due to their non-degradability and the persistent accumulation of plastic waste. It is essential to develop biodegradable and sustainable alternatives with favorable mechanical properties. Here, we developed a dilute-solution-based strategy that enables the facile and scalable production of high strength sustainable nanocomposites with multicomponent synergistic reinforcement. Owing to the shear-flow-induced nanosheets alignment and strong interfacial interactions, the nanocomposites achieve outstanding mechanical properties, with a high tensile strength of 566.9 ± 13.5 MPa. Moreover, these nanocomposites possess electromechanical stability and thermal stability, and can fully biodegrade within 30 days in natural soil. This strategy provides an effective pathway for the design of high-performance sustainable nanocomposites.

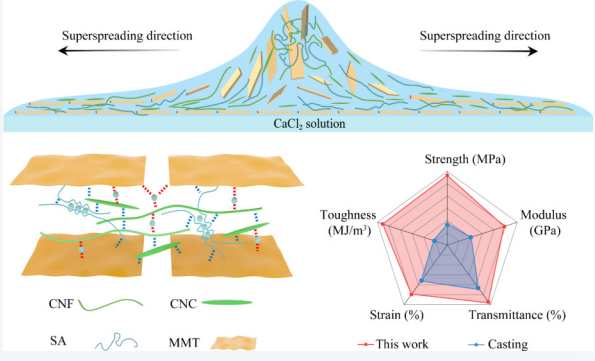

KEYWORDS: high strength, nanocomposite, superspreading, mechanical properties, sustainable

1 Introduction

Petroleum-based plastics have been extensively utilized in modern industry and daily life due to their low cost, processability, and excellent physical properties [1–3]. However, the persistent accumulation of plastic waste, particularly microplastics, causes ecological risks and threatens human health through bioaccumulation [4–6]. Therefore, it is crucial to develop biodegradable materials to replace existing petroleum-based plastic products [7]. Naturally derived polymers such as cellulose, chitosan, and alginate offer an attractive solution, owing to their abundance, renewability, and biodegradability [8–10]. But it remains a significant challenge to produce these biopolymer materials with excellent mechanical properties that meet the needs of practical applications.

Biomimetic design is an effective method to improve mechanical properties of materials [11–14]. And numerous successful cases of improving mechanical properties have been realized through imitating the hierarchical structure of biomaterials at multiple scales [15, 16]. In particular, the brick-and-mortar architecture of nacre, which consists of highly ordered inorganic calcium carbonate nanosheets and organic matrixes, offers a powerful design principle for fabricating high-performance nanocomposites [17, 18]. Many assembly strategies, such as casting [19–21], vacuum filtration [22, 23], and layer-by-layer [24–26], have been widely reported and demonstrated to be efficient approaches to fabricate high-performance nacre-inspired materials. However, for complex multicomponent systems, the above methods are prone to the aggregation of nanofillers during the depletion of solvents, resulting in decreased mechanical properties. Therefore, how to fabricate nanocomposites with complex multicomponent systems remains a difficult problem.

Herein, we present a multicomponent synergistic reinforcement strategy based on shear-flow-induced nanosheet alignment and rapid *in situ* crosslinking to enable the simple and scalable fabrication of high strength sustainable nanocomposites. The superspreading of dilute solutions on superhydrophilic surfaces generates strong shear forces which drive the ordered alignment of

Received: December 11, 2025; **Revised:** January 23, 2026
Accepted: January 25, 2026

✉Address correspondence to zhaochuangqi@ustc.edu.cn

nanosheets into a nacre-like layered structure. Ionic crosslinking was simultaneously introduced to stabilize the aligned structure and prevent aggregation of nanofillers during the depletion of solvents. In addition, strong interfacial interactions among the multiple components contributed to a synergistic enhancement of the mechanical properties. The resulting nanocomposites exhibit remarkable mechanical properties. Specifically, they possess a tensile strength of 566.9 ± 13.5 MPa, surpassing many reported sustainable nanocomposites and commercial plastics. Moreover, these nanocomposites demonstrate electromechanical stability and thermal stability and achieve complete biodegradation in natural soil within 30 days, highlighting their potential as sustainable alternatives to conventional plastics.

2 Experimental

2.1 Materials

Cellulose nanofiber (CNF) and cellulose nanocrystal (CNC) were acquired from Shanghai ScienceK Nanotechnology Co., Ltd. Montmorillonite (MMT) was purchased from Nanocor. Sodium alginate (SA) was obtained from Shanghai Macklin Biochemical Co., Ltd. Calcium chloride ($CaCl_2$) was purchased from Sinopharm Chemical Reagent Co., Ltd. All reagents were used as received. Deionized water was the solvent in all experiments.

2.2 Preparation of reaction solutions

Firstly, the dispersion of nanofillers (MMT, CNC, and CNF) and SA solution were prepared. MMT was exfoliated through mechanical stirring by dispersing the powder in deionized water and maintaining the suspension overnight, resulting in a 2 wt.% nanosheet dispersion. A transparent CNC dispersion (2 wt.%) was prepared by dispersing dry CNC powder in deionized water followed by overnight stirring. The purchased gel CNF dispersion was diluted with deionized water and stirred for 5 h to obtain a CNF dispersion (1 wt.%). SA solution (2 wt.%) was obtained by dissolving SA powder in deionized water followed by continuous stirring overnight. These solutions were subsequently added to deionized water to prepare reaction mixtures with varying weight percentages of polymer and nanofiller. To achieve homogeneous reaction solutions, the mixed solution was sonicated for 10 min to remove the bubbles.

2.3 Preparation of nanocomposites by superspreading method

Firstly, 1 M $CaCl_2$ aqueous solution was uniformly applied onto the surface of the microfiltration membrane to render it superhydrophilic. Subsequently, the prepared mixed reaction solution was gently poured onto the membrane surface. Upon contact with the superhydrophilic substrate, the solution droplets rapidly superspreaded, during which strong shear forces were generated, inducing the in-plane alignment of nanosheets. Simultaneously, Ca^{2+} ions diffused from the membrane surface into the reaction solution, triggering rapid *in situ* ionic crosslinking and converting the liquid film into a mechanically stable hydrogel. The microfiltration membrane was transferred to a water bath and the gel film was easily separated. Finally, the gel film was dried at 60 °C for 5 h to obtain the nanocomposite.

2.4 Preparation of nanocomposites by casting method

The mixed reaction solution was placed in a petri dish and dried at room temperature for 3 days. The nanocomposites were obtained after stripping.

2.5 Characterization

2.5.1 Microstructure characterizations

Atomic force microscopy (AFM) was performed using a Bruker Multimode scanning probe microscope operated in tapping mode with a scan rate of 1 Hz. The morphology of the nanocomposites was characterized by scanning electron microscopy (SEM, Quattro S, Thermo Fisher) at 10 kV. Transmission electron microscopy (TEM) images were obtained using an HT7700 at 100 kV.

2.5.2 Wide-angle X-ray scattering (WAXS) characterizations

The WAXS samples were prepared by cutting rectangular specimens (5 mm × 20 mm). Data were collected using a SAXS/WAXS instrument (Xeuss, Xenocs, France) employing Cu Kα radiation (λ = 1.54 Å), with the detector positioned 55.00 mm from the sample. A Pilatus3 R 300K detector (Dectris, Switzerland) captured the scattering signals. Two-dimensional diffraction patterns were processed into one-dimensional profiles via Debye–Scherrer ring integration using Foxtrot software. The azimuthal angle plots were fitted using a Maier–Saupe distribution function [26]

$$I = I_0 + A\exp[\omega\cos^2(\varphi - \varphi_0)] \quad (1)$$

where I_0 is the free baseline intensity, φ_0 is the azimuth at the position of the maximal intensity, φ is the azimuth, and ω defines the distribution width. The curve fitting of the Maier–Saupe function to the azimuthal angle plot provided values for I_0, A, and ω. The orientation order parameter f was then calculated through the following equation

$$f = \frac{\int_{-1}^{1} P_2(\cos\varphi)\exp(\omega\cos^2\varphi)\mathrm{d}(\cos\varphi)}{\int_{-1}^{1}\exp(\omega\cos^2\varphi)\mathrm{d}(\cos\varphi)} \quad (2)$$

where the function $P_2(\cos\varphi)$ is the second-order Legendre polynomial of $\cos\varphi$, often referred to as the Hermans orientation function

$$P_2(\cos\varphi) = \frac{1}{2}(3\cos^2\varphi - 1) \quad (3)$$

2.5.3 Spectral analysis

Fourier transform infrared (FTIR) spectroscopy spectra of the samples at different stages were measured using a NICOLET iN10 FTIR spectrometer in attenuated total reflectance (ATR) mode with a frequency range of 4000–525 cm^{-1} at a resolution of 0.5 cm^{-1} with a total of 32 scans. The ultraviolet–visible–near-infrared spectrometer (UV-3600i PLUS, Shimadzu) was employed to record the light transmittance of hydrogel in the wavelength range of 400–800 nm. Zeta potential tests were performed using the Malvern Zetasizer NANO ZSE under the condition of pH = 7.

2.5.4 Mechanical tests

Tensile tests were carried out using a Mark-10 ESM303 universal testing machine operated in stretch mode at room temperature. Prior to mechanical testing, all specimens were first dried in an oven at 60 °C under atmospheric pressure for 5 h to remove residual moisture and then equilibrated at 25 °C and 10% relative

humidity for 48 h to ensure a consistent moisture content. The specimens were cut into rectangular strips with a width of 1 mm and a length of 20 mm. Tensile measurements were conducted at a constant loading rate of 0.5 mm·min^{-1} until failure. For each nanocomposite composition, 8–10 specimens were tested to ensure statistical reliability. After testing, the thickness of each specimen was determined by scanning electron microscopy and used for accurate stress calculation.

2.5.5 *Porosity calculation*

The volume fraction of porosity (V_p) was calculated from mass density measurements as follows

$$V_p = 1 - \frac{\rho}{\rho_0} \quad (4)$$

where ρ and ρ_0 are the density of MCCS nanocomposites and the theoretical density of MCCS nanocomposites without voids, respectively. The theoretical densities of MCCS nanocomposites without any voids are obtained based on the theoretical densities of MMT nanosheet, CNC, CNF, and SA, and their composition ratios.

2.5.6 *Swelling tests*

Nanocomposite specimens were cut into 2 mm × 2 mm squares and immersed in water for varying durations to monitor changes in sample size. The swelling ratio (SR) was calculated as follows

$$\mathrm{SR}\,(\%) = \frac{S_1 - S_0}{S_0} \times 100 \quad (5)$$

where S_1 is the area of swollen samples and S_0 is the area of the dried samples.

2.5.7 *Thermal properties testing*

Thermogravimetric analysis (TGA) data were measured by the TG 209 F3 Tarsus instrument in a nitrogen atmosphere. A DMA 850 instrument was used to perform dynamic mechanical analysis (DMA) measurements. A pre-load of 0.05 N was applied before the measurement. The measurements were carried out at 1 Hz and 0.05% strain from 30 to 200 °C. The storage modulus and loss factor (tanδ) were measured.

2.5.8 *Biodegradation test in soil*

Nanocomposites were cut into 2 cm × 2 cm squares and buried at a depth of 3–5 cm in a natural soil environment. Degradability was assessed by tracking changes in sample morphology and dimensions over time, with observations recorded at three-day intervals. A minimum of three specimens, arranged in a randomized design, were tested under identical conditions to ensure reproducibility.

3 Results and discussion

3.1 Material design and fabrication strategy

The nanocomposites were constructed entirely from natural building blocks. MMT nanosheets, characterized by a high aspect ratio, high modulus, and natural abundance in soil, serve as ideal two-dimensional inorganic building blocks for constructing nacre-mimetic materials (Fig. S1 in the Electronic Supplementary Material (ESM)) [27, 28]. CNCs, one-dimensional nanorods derived from abundant plant cellulose, serve as reinforcing filler. They exhibit a high Young's modulus exceeding 150 GPa and possess abundant surface hydroxyl groups that facilitate the formation of strong hydrogen bonding networks [29, 30]. And CNFs form an entangled and ductile network which improves the toughness of the nanocomposites (Fig. S2 in the ESM) [31–33]. SA is a biodegradable polysaccharide which has oxygen-containing functional groups and can be cross-linked with Ca^{2+} to enhance interfacial interactions [34, 35]. These components form a hierarchically ordered brick-and-mortar structure.

The fabrication of the MMT-CNC-CNF-SA (abbreviated as MCCS) nanocomposites is illustrated in Fig. 1(a). First, uniformly dispersed MMT nanosheets were obtained through mechanical exfoliation. Subsequently they were mixed with CNC, CNF, and SA in different ratios and the mixed solution was then sonicated for 5 min to obtain a uniform dilute solution. Next, this dilute solution was poured onto a microfiltration membrane pre-coated with $CaCl_2$ and spread rapidly and entirely (defined as superspreading) (Fig. S3 and Video S1 in the ESM). The superspreading process provides a strong shear force that rapidly align the MMT nanosheets along the superspreading direction to form a highly ordered layered structure (Fig. 1(b)) [36–39]. Simultaneously, Ca^{2+} in the microfiltration membrane diffused from the membrane surface into the reaction solution, converting it into a hydrogel film through ionic crosslinking and effectively preserving the orientation structure [40, 41]. After the resulting hydrogel films were dried, uniform and transparent MCCS nanocomposites were obtained.

Furthermore, by extruding the reaction solution through a multichannel syringe, we achieved large-area production of the bioinspired nanocomposites (Fig. 1(c) and Fig. S4 in the ESM). The MCCS nanocomposites are self-supporting with intact structural integrity and exhibit macroscopic ductility, allowing them to be bent, wrapped, and even folded (Fig. 1(d) and Fig. S5 in the ESM). The MCCS nanocomposites display an ordered brick-and-mortar structure similar to natural nacre. Scanning electron microscopy (SEM) images reveal a close-packed lamellar morphology with well-ordered alignment of MMT nanosheets (Fig. 1(e)). The elemental distribution images by energy dispersive X-ray spectroscopy (EDS) analysis of the nanocomposites also demonstrated the uniform dispersion of nanosheets (Fig. S6 in the ESM). By adjusting the composition of the reaction solution, the thickness of nanocomposites can be tuned from approximately 2 to 9 μm (Fig. S7 in the ESM).

3.2 Mechanical properties of nanocomposites

Uniaxial tensile tests were conducted to evaluate the mechanical properties of the MCCS nanocomposites. For comparison, nanocomposites with different compositions, named as MMT-CNC (MC), MMT-CNC-CNF (MCC), and MMT-CNC-SA (MCS), were also tested to investigate the reinforcement of multiple components on mechanical properties (Fig. S8 in the ESM). Figures 2(a) and 2(b) present their typical stress–strain curves and the comparison of tensile strength, Young's modulus, and toughness. The corresponding mechanical properties are listed in Tables S1 and S2 in the ESM. The MC nanocomposites exhibit a relatively low tensile strength of 252.2 ± 17.5 MPa and a toughness of 1.7 ± 0.5 MJ·m^{-3}. Owing to the incorporation of a highly entangled CNF network, the tensile strength of the MCC nanocomposites increased to 1.41 times that of the MC nanocomposites, and the toughness increased to 2.24 times. And the MCCS nanocomposites show the superior mechanical

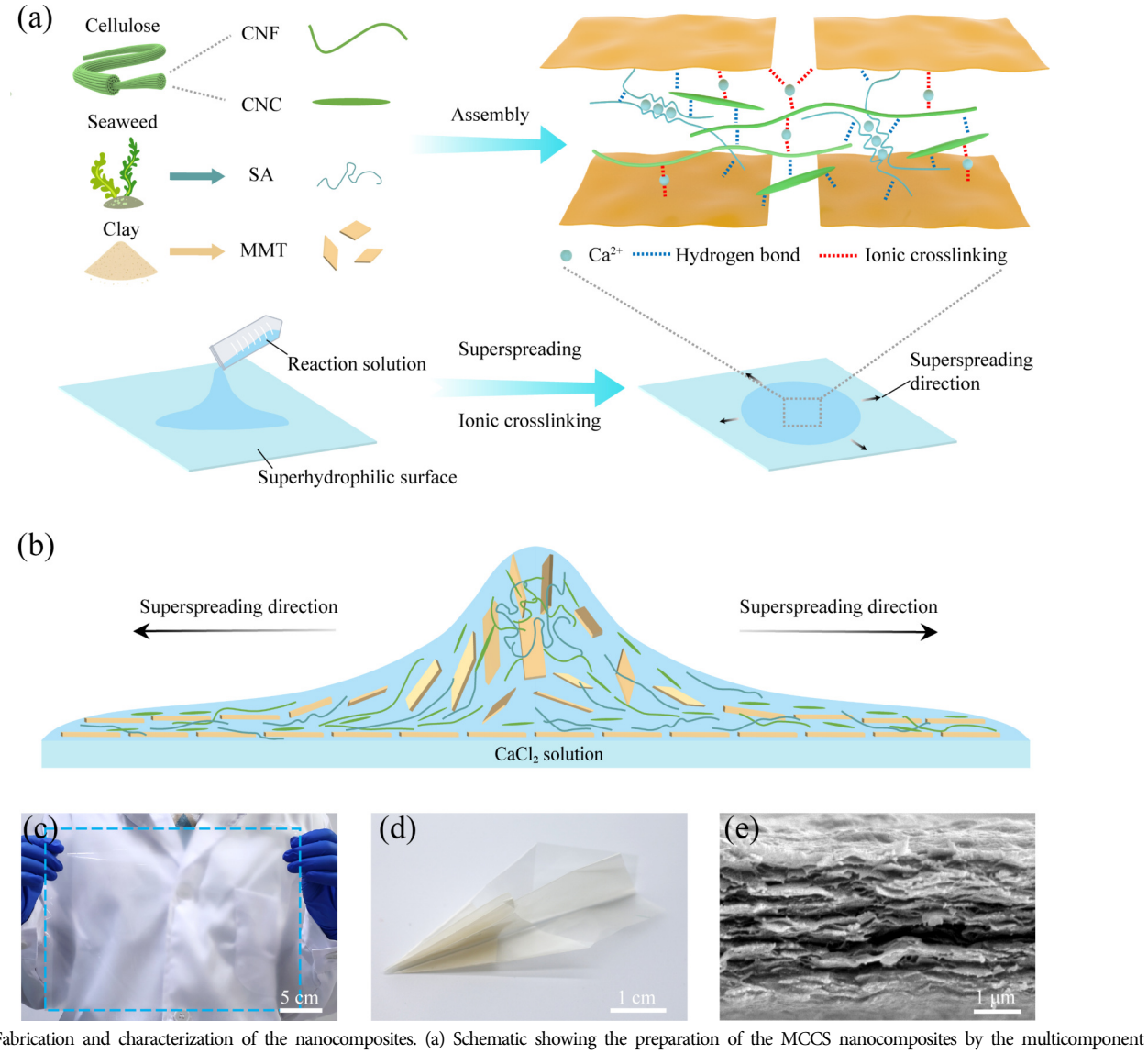

Figure 1 Fabrication and characterization of the nanocomposites. (a) Schematic showing the preparation of the MCCS nanocomposites by the multicomponent synergistic reinforcement strategy. (b) Schematic showing the reaction solution superspreading on the superhydrophilic surface. (c) Digital photo of the prepared large-area MCCS nanocomposites. (d) A paper plane model folded from the MCCS nanocomposites, demonstrating its excellent foldability. (e) The SEM cross-sectional image of the MCCS nanocomposites.

properties, with a tensile strength of 566.9 ± 13.5 MPa, a toughness of 16.3 ± 1.5 MJ·m^{-3}, a Young's modulus of 14.5 ± 0.8 GPa, and a failure strain of 4.9% ± 0.4%. Because voids in nanocomposites decrease mechanical performance, incorporating flexible SA molecular chains as filler and binder significantly reduces the porosity of the nanocomposites (Fig. S9 in the ESM) [34, 42]. By contrast, MCS nanocomposites exhibit markedly reduced mechanical properties, illustrating the indispensable contributions of both CNF and SA to mechanical properties reinforcement. As a result of these enhancements, an MCCS nanocomposite sample with a width of 2.5 mm and a thickness of 4 μm can lift a weight of 500 g without breaking (Fig. 2(c)). In summary, the MCCS nanocomposites we prepared have excellent mechanical properties, which exceed many reported sustainable nanocomposites (Fig. 2(d) and Table S4 in the ESM) and far outperform most commercial plastics (Fig. S10 in the ESM). Therefore, our MCCS nanocomposites provide sufficient mechanical properties for plastic replacement.

To reveal the strengthening mechanism of the MCCS nanocomposites, their fracture morphologies were carefully studied. The MCCS nanocomposites exhibit a densely packed layered architecture with curled fracture edges, revealing the pull-out of MMT nanosheets which contributes to energy dissipation during fracture (Fig. 2(e)). Additionally, the pull-out of CNC and CNF is observed, further enhancing the fracture energy dissipation (Fig. 2(f)). These nanofillers not only facilitate the energy absorption but also prevent the fracture propagation. Crack deflection is evident in the fracture surfaces of the MCCS nanocomposites (Fig. 2(g)). This deflection mechanism is acknowledged as the most important reinforcement mechanism in nacre, as it redirects the crack path, thereby promoting the dissipation of fracture energy [43]. Based on the fracture morphology of the nanocomposites, a crack extension model is proposed to reveal the synergistic strengthening (Fig. 2(h)). Initially, the SA matrix deforms and the MMT starts to slide and deflect the crack under tensile stress. As stretching continues, the propagation

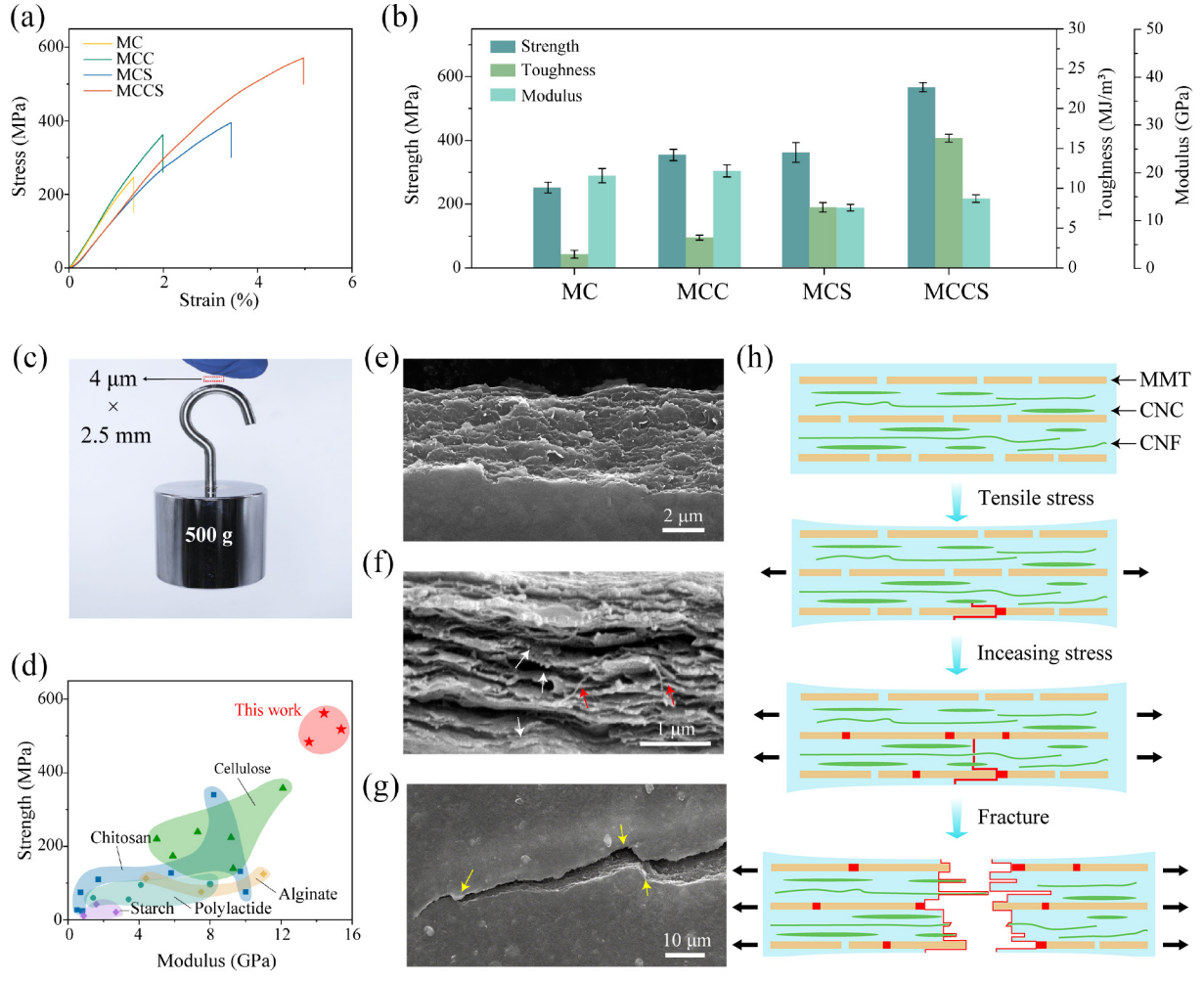

Figure 2 Mechanical properties of the nanocomposites. (a) Tensile stress–strain curves of MC, MCC, MCS, and MCCS nanocomposites. (b) The strength, toughness, and Young's modulus of MC, MCC, MCS, and MCCS nanocomposites. (c) The MCCS nanocomposite with a thickness of 4 μm and a width of 2.5 mm lifting 500 g weights without fracture. (d) Comparison of the tensile strength and Young's modulus of MCCS nanocomposites with those reported sustainable nanocomposites. A summary of the data used is provided in Table S4 in the ESM. (e) Inclined view of the fracture surface of the MCCS nanocomposites. (f) CNC (white arrow) and CNF (red arrow) pull-out on fracture surface. (g) Top view of MCCS nanocomposites in the fracture zone. The crack propagated in a deflected direction (yellow arrow). (h) The proposed fracture mechanism of the MCCS nanocomposites. Under tensile stress, the SA matrix deforms and the MMT starts to slide and deflect the crack. CNC and CNF bridge the crack and resist MMT sliding, thus activating potential slip sites for the next multiple MMT nanosheets. The nanocomposite eventually fails in MMT pull-out and nanocellulose pull-out modes.

of these microcracks will be hindered by the nanocellulose. The increased stress is then transmitted to the subsequent MMT nanosheet layer, thereby activating the sliding of neighboring nanosheets. As the crack extends, the accumulation of crack deflection and the activation of potential sliding sites gradually lead to fracture. The strain hardening shown in the nonlinear stress–strain curve also reflects this deformation process (Fig. S8(d) in the ESM) [21].

3.3 Interfacial interactions and nanosheets alignment

To investigate the influence of interfacial interactions on mechanical properties, attenuated total reflectance Fourier transform infrared (ATR-FTIR) spectroscopy was performed on the nanocomposites (Fig. 3(a)). The broad absorption band at 3344 cm^{-1} in the MC spectrum corresponds to the O–H stretching vibration. In comparison, the O–H stretching peaks showed a significant red shift to 3336 cm^{-1} in MCC and 3324 cm^{-1} in MCCS, indicating the formation of strong hydrogen bonding interactions in the nanocomposites [37, 40]. In the FTIR spectrum of MCCS, distinct absorption peaks appear at 1597 and 1424 cm^{-1}, attributed to the asymmetric and symmetric stretching vibrations of carboxyl groups on SA and CNF, respectively [34]. The non-crosslinked nanocomposites show corresponding peaks at 1601 and 1415 cm^{-1}, suggesting coordination between Ca^{2+} and the carboxyl groups [44–46]. Additionally, we measured the zeta potentials of MMT nanosheets and CNC aqueous dispersions (Fig. 3(b)). The zeta potentials of MMT and CNC were −39.96 and −59.91 mV, respectively, indicating negative surface charges that promote stable aqueous dispersion. With the incorporation of Ca^{2+}, the zeta potentials of MMT and CNC increased to −23.76 and −22.61 mV, respectively, confirming the electrostatic interactions between Ca^{2+} and negative charges [47, 48]. These interfacial interactions contribute to the formation of a strong network that facilitates efficient stress transfer, thereby enhancing the mechanical properties of the nanocomposites. Given the inherent water instability of cellulose-based materials, swelling tests were performed on the MCCS nanocomposites (Fig. S11 in the ESM).

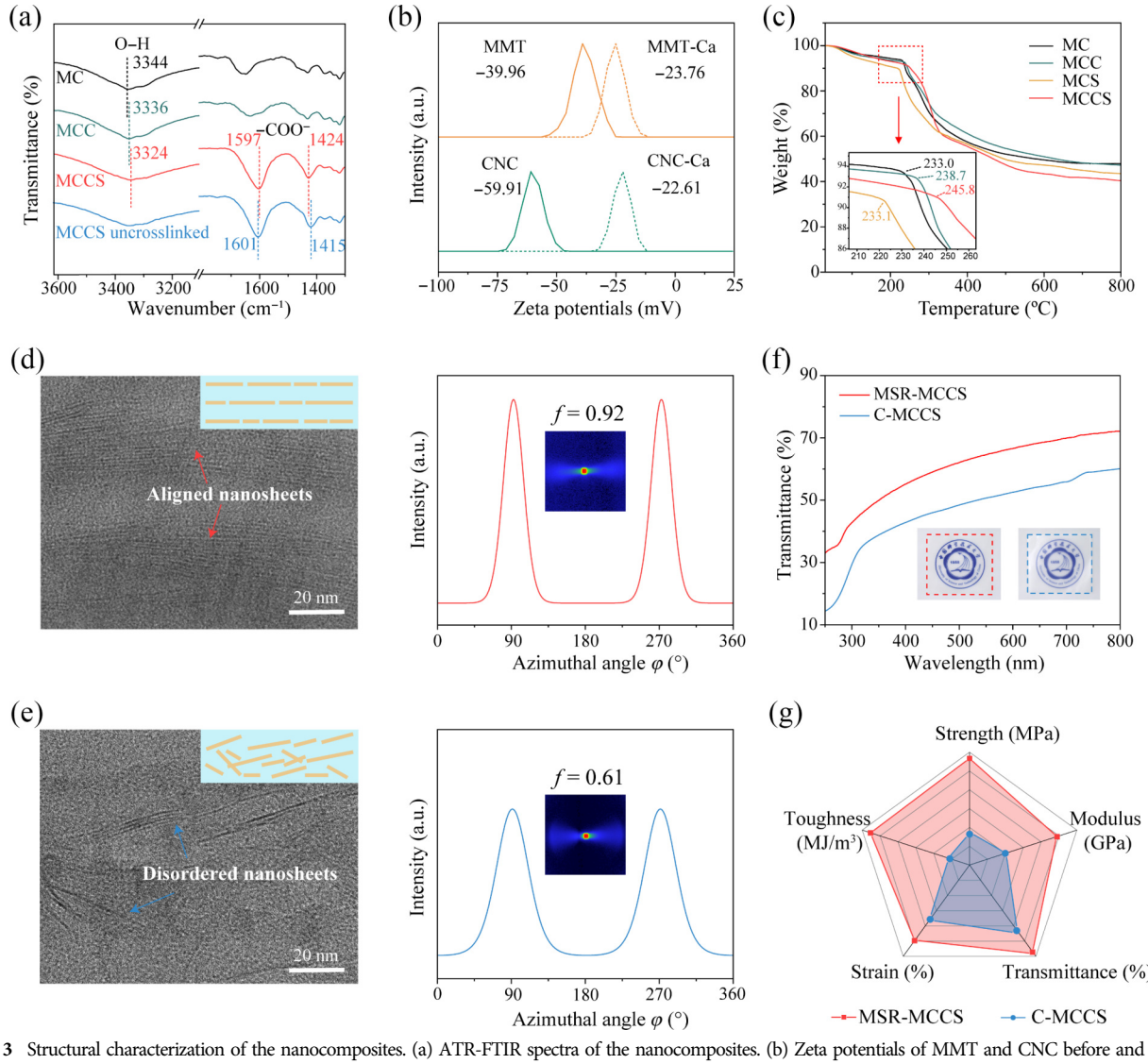

Figure 3 Structural characterization of the nanocomposites. (a) ATR-FTIR spectra of the nanocomposites. (b) Zeta potentials of MMT and CNC before and after the addition of Ca^{2+}. (c) TGA of the nanocomposites. (d) TEM image, 2D WAXS images, and φ plots for the MSR-MCCS nanocomposites. (e) TEM image, 2D WAXS images, and φ plots for the C-MCCS nanocomposites. (f) The transparency of the MSR-MCCS nanocomposites and C-MCCS nanocomposites. (g) A radial plot comparing the tensile strength, Young' s modulus, toughness, strain, and transmittance of different nanocomposites.

The results show that the crosslinked nanocomposites exhibited negligible changes after 3 h of immersion in water, while the uncrosslinked nanocomposites showed a swelling ratio up to 600% due to weak interfacial interactions [49]. In addition, thermogravimetric analysis (TGA) revealed that the MCCS nanocomposites decompose at 245.8 °C compared with 233 °C for the MC nanocomposite (Fig. 3(c)), further confirming enhanced interfacial interactions.

It is widely acknowledged that the outstanding mechanical properties of nacre-inspired nanocomposites depend not only on the interfacial interactions between the matrix and nanosheets, but also critically on the ordered alignment of the nanosheets [18, 36, 37]. The orientation of MMT nanosheets in MCCS nanocomposites was characterized using TEM and WAXS. Cross-sectional TEM images of MCCS nanocomposites prepared by the multicomponent synergistic reinforcement strategy (MSR-MCCS) reveal a highly ordered nanosheet alignment (Fig. 3(d)). In contrast, the nanocomposites made by casting method (C-MCCS) have randomly distributed MMT nanosheets (Fig. 3(e)). The two-dimensioanl (2D) WAXS patterns of MSR-MCCS nanocomposites display two intense diffuse spots in the equatorial direction, corresponding to distinct peaks at 90° and 270° in the φ distribution. The degree of nanosheet orientation was determined utilizing the Maier–Saupe orientation distribution function, resulting in orientation parameter (f) values ranging from 0.92 to 0.81, decreasing with the additional SA content (Fig. S12 in the ESM). These high f values confirm that the multicomponent synergistic reinforcement strategy can achieve highly ordered alignment of MMT nanosheets. By contrast, the C-MCCS nanocomposites present a comparatively flat φ plot and a low f (0.61), indicating the disordered distribution of MMT nanosheets. The aggregation of nanosheets was also observed in the C-MCCS nanocomposites, severely impairing their mechanical properties (Fig. S13 in the ESM). As a result, MSR-MCCS nanocomposites exhibit tensile strengths approximately four times greater than those of C-MCCS nanocomposites (Fig. S14 and Table S3 in the ESM). This notable enhancement highlights the critical role of nanosheet alignment in stress transfer. Furthermore, the ordered nanosheet

alignment reduces light scattering between the nanosheets, endowing the MSR-MCCS nanocomposites with higher transparency than C-MCCS nanocomposites (Fig. 3(f)) [50]. The above results fully demonstrate that the multicomponent synergistic reinforcement strategy has significant advantages over the casting method (Fig. 3(g)).

3.4 Electromechanical stability, thermal stability, and biodegradability

The MCCS nanocomposites can serve as a flexible substrate for electronic devices, on which conductive circuits are fabricated via screen printing of silver paste (Fig. 4(a)). Figure 4(b) shows the resistance change of the printed circuit at different bending angles. The resistance of the flexible substrate increases slightly from 36.5 to 38.9 Ω when bent from 0° to 150°, which fully reflects the excellent electromechanical stability of the substrate. Furthermore, the light-emitting diodes mounted on the flexible substrate remained steadily illuminated after circuit integration, confirming the conductivity and stability of the metallic ink (Fig. 4(c)). These results indicate that our MCCS nanocomposites fully meet the basic requirements for flexible substrate.

Dynamic mechanical analysis (DMA) was conducted on MCCS nanocomposites and several commercial plastics. As shown in Fig. 4(d), the MCCS nanocomposites exhibit a stable storage modulus of approximately 10 GPa over the temperature range of 30–200 °C, which is significantly higher and more stable than that of the tested plastics. The tanδ also remains low and stable over this range, signifying exceptional thermomechanical stability (Fig. 4(e)). More intuitively, the MCCS nanocomposites retained their structural integrity at 200 °C through the hot plate experiment, while the tested commercial plastics softened and deformed (Fig. 4(f)). These results indicate that the MCCS nanocomposites have excellent thermal stability, ensuring their potential use in advanced applications [51].

To evaluate the environmental degradability of the MCCS nanocomposites, soil burial tests were investigated through recording variations in appearance and dimension over time (Fig. 4(g)). The results show minimal dimensional changes during the initial five days of burial, followed by an accelerated degradation rate. Then the nanocomposites completely degraded within only 30 days, leaving no visible residues (Fig. 4(h)). This rapid degradation highlights the excellent biodegradability of the MCCS nanocomposites, demonstrating the potential to decompose efficiently under natural conditions. Such performance not only minimizes the risk of environmental pollution but also aligns with

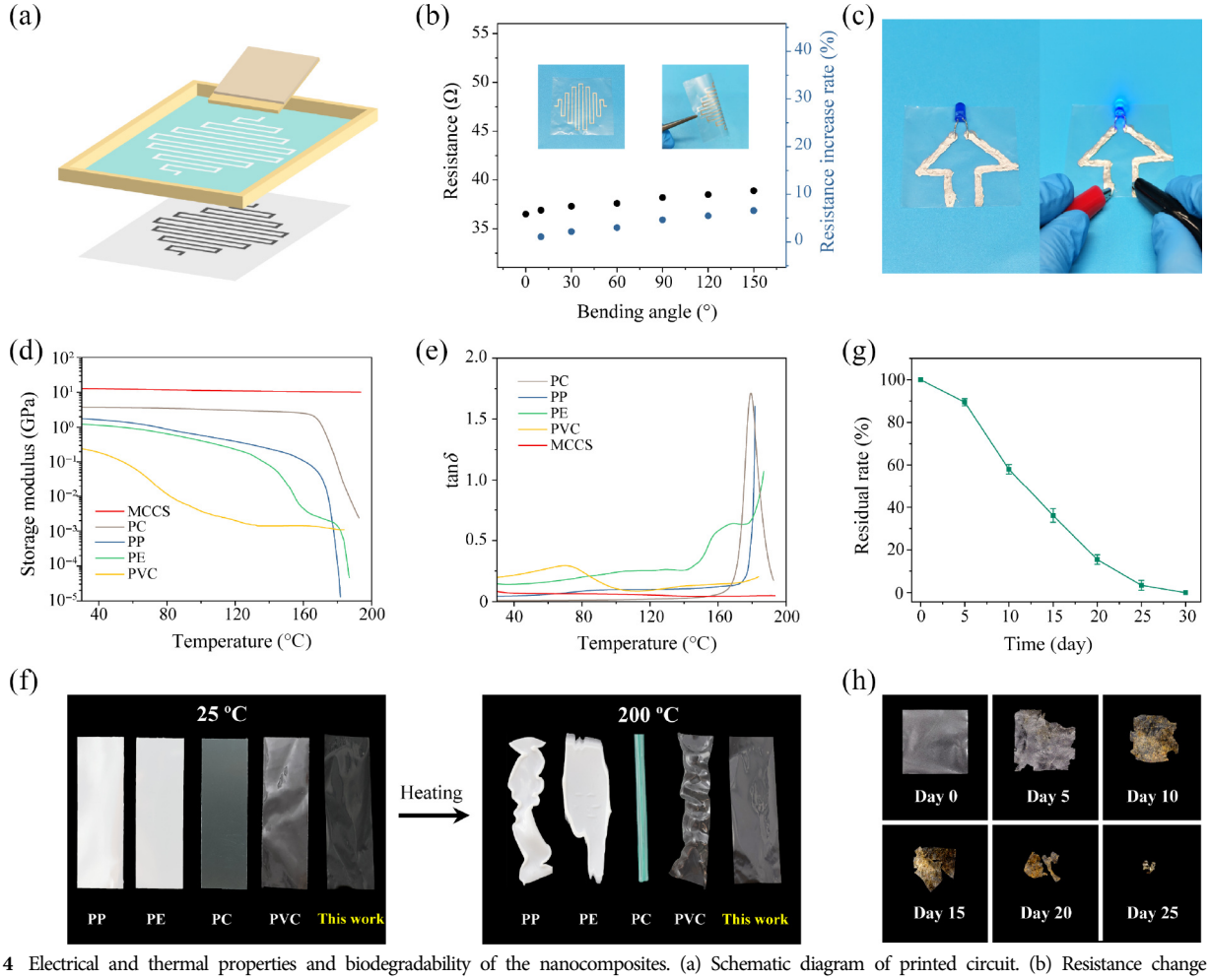

Figure 4 Electrical and thermal properties and biodegradability of the nanocomposites. (a) Schematic diagram of printed circuit. (b) Resistance change of the nanocomposite after printing circuit under different bending angles. (c) Photographs of a light-emitting diode illuminated via silver ink circuits. (d) Comparison of the storage modulus of the MCCS nanocomposites with that of some widely used plastics. (e) Comparison of the tanδ of the MCCS nanocomposites with that of some widely used plastics. (f) Photographs of the thermal stability comparison of the MCCS nanocomposites with some widely used plastics at 25 and 200 °C. (g) Residual rate of the MCCS nanocomposites buried in natural environment soil for different days. (h) Optical photographs of MCCS nanocomposites during soil burial biodegradation.

the principles of sustainable materials design.

4 Conclusions

In summary, we fabricated high strength sustainable nanocomposites through multicomponent synergistic reinforcement strategy. The layered structure formed by the ordered alignment of MMT nanosheets and strong interfacial interactions among the multiple components together result in the synergistic reinforcement mechanical properties, including a tensile strength of 566.9 ± 13.5 MPa, a toughness of 16.3 ± 1.5 $MJ·m^{-3}$, and a Young's modulus of 14.5 ± 0.8 GPa. Moreover, the nanocomposites exhibit outstanding electromechanical stability, thermal stability, and biodegradability, making them promising alternatives to conventional plastics. This strategy is expected to offer an effective route for the development of sustainable nanocomposites for plastic replacement.

Electronic Supplementary Material: Supplementary material (further details of sample characterizations) is available in the online version of this article at https://doi.org/10.26599/NR.2026.94908491.

Data availability

All data needed to support the conclusions in the paper are presented in the manuscript and the Electronic Supplementary Material. Additional data related to this paper may be requested from the corresponding author upon request.

Acknowledgements

This work was supported by CAS Hundred Talent Program (No. KJ2060007007), the Youth Fund of the National Natural Science Foundation of China (No. 22305244), the Start-up Funding for Suzhou Institute for Advanced Research, University of Science and Technology of China (No. KY2260080033), the Start-up Funding for University of Science and Technology of China (No. KY2060000233), and Suzhou Key Laboratory of Bioinspired Interfacial Science (No. SZ2024004). We thank the Physical and Chemical Analysis Center at Suzhou Institute for Advanced Research, University of Science and Technology of China, and Key Laboratory of Precision and Intelligent Chemistry, University of Science and Technology of China.

Declaration of competing interest

All the contributing authors report no conflict of interests in this work.

Author contribution statement

G. J. C.: Conceptualization, data curation, validation, methodology, investigation, formal analysis, writing – original draft. S. X. Y.: Methodology, software, validation, visualization. C. Q.: Software, validation, visualization. C. Z.: Investigation, software. Y. D.: Investigation, validation. Y. Z: Investigation, validation. C. Q. Z.: Project administration, funding acquisition, resources, supervision, writing – review & editing. L. J.: Supervision, methodology, validation. All the authors have approved the final manuscript.

Use of AI statement

None.

References

[1] Geyer, R.; Jambeck, J. R.; Law, K. L. Production, use, and fate of all plastics ever made. *Sci. Adv.* **2017**, *3*, e1700782.
[2] Gibb, B. C. Plastics are forever. *Nat. Chem.* **2019**, *11*, 394–395.
[3] Ghasemlou, M.; Adhikari, B.; Naebe, M.; Barrow, C. J. Bioengineering strategies to promote plastic circularity. *Nat. Rev. Bioeng.* **2025**, *3*, 353–354.
[4] Rochman, C. M.; Browne, M. A.; Halpern, B. S.; Hentschel, B. T.; Hoh, E.; Karapanagioti, H. K.; Rios-Mendoza, L. M.; Takada, H.; Teh, S.; Thompson, R. C. Classify plastic waste as hazardous. *Nature* **2013**, *494*, 169–171.
[5] Lau, W. W. Y.; Shiran, Y.; Bailey, R. M.; Cook, E.; Stuchtey, M. R.; Koskella, J.; Velis, C. A.; Godfrey, L.; Boucher, J.; Murphy, M. B. et al. Evaluating scenarios toward zero plastic pollution. *Science* **2020**, *369*, 1455–1461.
[6] Pang, Q. T.; Wu, P. P.; Galgani, L.; Wang, X. L.; Zhang, Z. M.; Yuan, T. F.; Wang, H. K.; Zhang, Y. X. The potential impacts of plastic on the marine carbon cycle. *Nat. Sustain.* **2025**, *8*, 1154–1163.
[7] Zhu, Y. Q.; Romain, C.; Williams, C. K. Sustainable polymers from renewable resources. *Nature* **2016**, *540*, 354–362.
[8] Mohanty, A. K.; Vivekanandhan, S.; Pin, J. M.; Misra, M. Composites from renewable and sustainable resources: Challenges and innovations. *Science* **2018**, *362*, 536–542.
[9] Li, C. M.; Wu, J. Q.; Shi, H. Y.; Xia, Z. Y.; Sahoo, J. K.; Yeo, J. J.; Kaplan, D. L. Fiber-based biopolymer processing as a route toward sustainability. *Adv. Mater.* **2022**, *34*, 2105196.
[10] Chen, L.; Yu, L.; Qi, L. H.; Eichhorn, S. J.; Isogai, A.; Lizundia, E.; Zhu, J. Y.; Chen, C. J. Cellulose nanocomposites by supramolecular chemistry engineering. *Nat. Rev. Mater.* **2025**, *10*, 728–749.
[11] Li, L.; Cheng, Q. F. Anisotropic thermally conductive films based on two-dimensional nanomaterials. *Interdiscip. Mater.* **2024**, *3*, 847–864.
[12] Liu, Y. F.; Hou, X. Y.; Song, Y. L.; Li, M. Z. Bioinspired reflective display based on photonic crystals. *Interdiscip. Mater.* **2024**, *3*, 54–73.
[13] Wang, Q.; Hu, L. S.; Wang, X. Y.; Tang, R. K. Expanding from materials to biology inspired by biomineralization. *Interdiscip. Mater.* **2024**, *3*, 165–188.
[14] Kong, S. W.; Zhao, C. Q.; Sun, Y. Z.; Huang, J.; Zhang, L. H.; Ru, Y. F.; Zhou, H. S.; Zhou, T. X.; Liu, M. J. Large-area, high-strength cellulose nanocomposites enhanced by confined polymer nanocrystallization in Bouligand structures. *Matter* **2024**, *7*, 2250–2264.
[15] Wegst, U. G. K.; Bai, H.; Saiz, E.; Tomsia, A. P.; Ritchie, R. O. Bioinspired structural materials. *Nat. Mater.* **2015**, *14*, 23–36.
[16] Huang, W.; Restrepo, D.; Jung, J. Y.; Su, F. Y.; Liu, Z. Q.; Ritchie, R. O.; Mckittrick, J.; Zavattieri, P.; Kisailus, D. Multiscale toughening mechanisms in biological materials and bioinspired designs. *Adv. Mater.* **2019**, *31*, 1901561.
[17] Zhao, H. W.; Yang, Z.; Guo, L. Nacre-inspired composites with different macroscopic dimensions: Strategies for improved mechanical performance and applications. *NPG Asia Mater.* **2018**, *10*, 1–22.
[18] Li, Y. C.; Lian, W. W.; Cheng, Q. F. High-performance nacre-inspired 2D carbon-based nanocomposites. *Adv. Mater.* **2025**, *37*, e2501932.
[19] Das, P.; Malho, J. M.; Rahimi, K.; Schacher, F. H.; Wang, B. C.; Demco, D. E.; Walther, A. Nacre-mimetics with synthetic nanoclays up to ultrahigh aspect ratios. *Nat. Commun.* **2015**, *6*, 5967.
[20] Mu, Z. C.; Wu, S. F.; Huang, X. B.; Zhang, W.; Yi, J. Y.; Jiang, N. J. High Elongation and Transparent Nacre-Inspired PVA/MMT Nanocomposites. *Macromol. Rapid Commun.* **2021**, *42*, 2100229.
[21] Wang, J. F.; Cheng, Q. F.; Lin, L.; Jiang, L. Synergistic toughening of bioinspired poly(vinyl alcohol)-clay-nanofibrillar cellulose artificial nacre. *ACS Nano* **2014**, *8*, 2739–2745.

[22] Liu, Y. X.; Yu, S. H.; Bergström, L. Transparent and flexible nacre-like hybrid films of aminoclays and carboxylated cellulose nanofibrils. *Adv. Funct. Mater.* **2018**, *28*, 1703277.
[23] Yang, X.; Li, L. W.; Nishiyama, Y.; Reid, M. S.; Berglund, L. A. Processing strategy for reduced energy demand of nanostructured CNF/clay composites with tailored interfaces. *Carbohydr. Polym.* **2023**, *312*, 120788.
[24] Podsiadlo, P.; Kaushik, A. K.; Arruda, E. M.; Waas, A. M.; Shim, B. S.; Xu, J. D.; Nandivada, H.; Pumplin, B. G.; Lahann, J.; Ramamoorthy, A. et al. Ultrastrong and stiff layered polymer nanocomposites. *Science* **2007**, *318*, 80–83.
[25] Qin, S.; Pour, M. G.; Lazar, S.; Köklükaya, O.; Gerringer, J.; Song, Y. X.; Wågberg, L.; Grunlan, J. C. Super gas barrier and fire resistance of nanoplatelet/nanofibril multilayer thin films. *Adv. Mater. Interfaces* **2019**, *6*, 1801424.
[26] Chen, Q.; Jamilpanah, L.; Künniger, T.; Furrer, R.; Song, Q.; Zhang, K.; Chumakov, A.; Harder, C.; Bulut, Y.; Müller-Buschbaum, P. et al. Reconfigurable soft actuators constructed via layer-by-layer assembly. *Adv. Mater. Interfaces* **2025**, *12*, 2500269.
[27] Li, L. W.; Maddalena, L.; Nishiyama, Y.; Carosio, F.; Ogawa, Y.; Berglund, L. A. Recyclable nanocomposites of well-dispersed 2D layered silicates in cellulose nanofibril (CNF) matrix. *Carbohydr. Polym.* **2022**, *279*, 119004.
[28] Gao, Y. S.; Qiao, Z. L.; Zhang, L.; Shi, L. High-performance proton exchange membrane with vertically aligned montmorillonite nanochannels. *Small* **2025**, *21*, e2409192.
[29] Fernández-Santos, J.; Valls, C.; Cusola, O.; Roncero, M. B. Composites of cellulose nanocrystals in combination with either cellulose nanofibril or carboxymethylcellulose as functional packaging films. *Int. J. Biol. Macromol.* **2022**, *211*, 218–229.
[30] Benítez, A. J.; Walther, A. Cellulose nanofibril nanopapers and bioinspired nanocomposites: A review to understand the mechanical property space. *J. Mater. Chem. A* **2017**, *5*, 16003–16024.
[31] Yang, H. B.; Yue, X.; Liu, Z. X.; Guan, Q. F.; Yu, S. H. Emerging sustainable structural materials by assembling cellulose nanofibers. *Adv. Mater.* **2025**, *37*, 2413564.
[32] Wang, S. N.; Zhang, L. L.; Khan, K. A.; Ullah, M. W.; Fan, Y. M.; Wang, Z. G. Deep eutectic solvents as a "multifunctional operating platform" for nanocellulose production and modification: A review on sustainable composite advancements. *Mater. Sci. Eng.: R: Rep.* **2025**, *165*, 101025.
[33] Wei, J. J.; Zhu, C. L.; Zeng, Z. H.; Pan, F.; Wan, F. Q.; Lei, L. W.; Nyström, G.; Fu, Z. Y. Bioinspired cellulose-integrated MXene-based hydrogels for multifunctional sensing and electromagnetic interference shielding. *Interdiscip. Mater.* **2022**, *1*, 495–506.
[34] Li, D. H.; Han, Z. M.; Shao, M.; Jiao, Z. J.; Gao, C.; Sun, W. B.; Liu, Z. X.; Yang, K. P.; Guan, Q. F.; Yu, S. H. A robust, biodegradable, and fire-retardant cellulose nanofibers-based structural material fabricated from natural sargassum. *Adv. Mater.* **2025**, *37*, 2417617.
[35] Zhang, H.; Xu, T.; Zhang, M.; Wang, X.; Qi, J. J.; Wang, Y. X.; Du, H. S.; Zhu, L. Y.; Liu, K.; Zhang, K. et al. Natural biomass hydrogels for intelligent sensing: From component crosslinking engineering to stimuli-responsive mechanisms. *eScience*, in press, https://doi.org/10.1016/j.esci.2025.100505.
[36] Zhao, C. Q.; Zhang, P. C.; Zhou, J. J.; Qi, S. H.; Yamauchi, Y.; Shi, R. R.; Fang, R. C.; Ishida, Y.; Wang, S. T.; Tomsia, A. P. et al. Layered nanocomposites by shear-flow-induced alignment of nanosheets. *Nature* **2020**, *580*, 210–215.
[37] Zhou, T. X.; Zhao, C. Q.; Liu, Y. H.; Huang, J.; Zhou, H. S.; Nie, Z. D.; Fan, M.; Zhao, T. Y.; Cheng, Q. F.; Liu, M. J. Large-area ultrastrong and stiff layered MXene nanocomposites by shear-flow-induced alignment of nanosheets. *ACS Nano* **2022**, *16*, 12013–12023.
[38] Liu, X. J.; Ma, L. L.; Zhou, C.; Liu, L. X.; Qian, C.; Zhao, C. Q.; Jiang, L. Microgroove-based continuous-spinning of ultra-strong polyelectrolyte nanocomposite fibers with aligned polymer chains and nanosheets. *Interdiscip. Mater.* **2025**, *4*, 333–342.
[39] Zhang, Y.; Liu, L. X.; Yin, S. X.; Zhou, C.; Ding, Y.; Che, G. J.; Zhao, C. Q. Underwater high strength and tough polyvinyl alcohol-polyacrylic acid hydrogel. *Adv. Funct. Mater.* **2025**, *35*, 2503023.
[40] Yin, S. X.; Ding, Y.; Zhang, Y.; Zhou, C.; Qian, C.; Che, G. J.; Zhao, C. Q.; Jiang, L. Superstrong and transparent hydrogels with homogeneous multiple networks. *Macromolecules* **2025**, *58*, 4357–4364.
[41] Zhou, C.; Zhao, C. Q.; Nie, Z. D.; Zhou, T. X.; Kong, S. W.; Sun, Y. Z.; Qian, C.; Zhao, T. Y.; Liu, M. J. Large-area layered membranes with precisely controlled nano-confined channels. *Angew. Chem.* **2024**, *136*, e202410441.
[42] Wan, S. J.; Li, X.; Chen, Y.; Liu, N. N.; Du, Y.; Dou, S. X.; Jiang, L.; Cheng, Q. F. High-strength scalable MXene films through bridging-induced densification. *Science* **2021**, *374*, 96–99.
[43] Wang, R. Z.; Wen, H. B.; Cui, F. Z.; Zhang, H. B.; Li, H. D. Observations of damage morphologies in nacre during deformation and fracture. *J. Mater. Sci.* **1995**, *30*, 2299–2304.
[44] Cui, H. L.; Pan, N.; Fan, W. X.; Liu, C. Z.; Li, Y. H.; Xia, Y. Z.; Sui, K. Y. Ultrafast fabrication of gradient nanoporous all-polysaccharide films as strong, superfast, and multiresponsive actuators. *Adv. Funct. Mater.* **2019**, *29*, 1807692.
[45] Papageorgiou, S. K.; Kouvelos, E. P.; Favvas, E. P.; Sapalidis, A. A.; Romanos, G. E.; Katsaros, F. K. Metal-carboxylate interactions in metal-alginate complexes studied with FTIR spectroscopy. *Carbohydr. Res.* **2010**, *345*, 469–473.
[46] Dong, H.; Snyder, J. F.; Williams, K. S.; Andzelm, J. W. Cation-induced hydrogels of cellulose nanofibrils with tunable moduli. *Biomacromolecules* **2013**, *14*, 3338–3345.
[47] Doustdar, F.; Olad, A.; Ghorbani, M. Effect of glutaraldehyde and calcium chloride as different crosslinking agents on the characteristics of chitosan/cellulose nanocrystals scaffold. *Int. J. Biol. Macromol.* **2022**, *208*, 912–924.
[48] Kumar, A.; Lee, Y.; Kim, D.; Rao, K. M.; Kim, J.; Park, S.; Haider, A.; Lee, D. H.; Han, S. S. Effect of crosslinking functionality on microstructure, mechanical properties, and *in vitro* cytocompatibility of cellulose nanocrystals reinforced poly(vinyl alcohol)/sodium alginate hybrid scaffolds. *Int. J. Biol. Macromol.* **2017**, *95*, 962–973.
[49] Lee, K.; Jeon, Y.; Kim, D.; Kwon, G.; Kim, U. J.; Hong, C.; Choung, J. W.; You, J. Double-crosslinked cellulose nanofiber based bioplastic films for practical applications. *Carbohydr. Polym.* **2021**, *260*, 117817.
[50] Yu, X. D.; Fan, J. H.; Zheng, S. Q.; Ma, L. L.; Liu, X. J.; Wu, Y.; Zhao, C. Q.; Jiang, L. High strength chitosan-based nanocomposites with aligned nanosheets and crosslinked networks. *Nanoscale* **2025**, *17*, 3105–3113.
[51] Guan, Q. F.; Yang, H. B.; Han, Z. M.; Ling, Z. C.; Yu, S. H. An all-natural bioinspired structural material for plastic replacement. *Nat. Commun.* **2020**, *11*, 5401.